Pre- and post-irradiation performance of FBK 3D silicon pixel detectors for CMS

DOI:10.1016/j.nima.2014.06.029

(Article begins on next page)

Pre- and post-irradiation performance of FBK 3D silicon pixel detectors for CMS

A. Krzywda[a,*], E. Alagoz[a], M. Bubna[a], M. Obertino[b,d], A. Solano[c,d], K. Arndt[a], L. Uplegger[e], G. F. Dalla Betta[g], M. Boscardin[f], J. Ngadiuba[h], R. Rivera[e], D. Menasce[h], L. Moroni[h], S. Terzo[h], D. Bortoletto[a], A. Prosser[e], J. Adreson[e], S. Kwan[e], I. Osipenkov[j], G. Bolla[a], C. M. Lei[e], I. Shipsey[a], P. Tan[e], N. Tran[e], J. Chramowicz[e], J. Cumalat[i], L. Perera[l], M. Povoli[g], R. Mendicino[g], A. Vilela Pereira[k], R. Brosius[a], A. Kumar[e], S. Wagner[i], F. Jensen[i], S. Bose[m], S. Tentindo[n]

[a] *Purdue University, Department of Physics and Astronomy, West Lafayette, IN 47907-2036, USA*
[b] *Università del Piemonte Orientale, Novara, Italy*
[c] *Università di Torino, Torino, Italy*
[d] *INFN, Sezione di Torino, Torino, Italy*
[e] *Fermi National Accelerator Laboratory, Batavia, IL 60510-5011, USA*
[f] *Centro per Materiali e i Microsistemi Fondazione Bruno Kessler (FBK),Trento, Via Sommarive 18, I-38123 Povo di Trento (TN), Italy*
[g] *TIFPA INFN and Dipartimento di Ingegneria Industriale, Università di Trento, Via Sommarive 9, I-38123 Povo di Trento (TN), Italy*
[h] *Università di Milano-Bicocca, Milan, Italy*
[i] *University of Colorado-Boulder, Department of Physics, Boulder, CO 80309, USA*
[j] *Texas A&M University, Department of Physics, College Station, TX 77843, USA*
[k] *Instituto di Fisica, Universidade do Estado do Rio de Janeiro (UERJ), Rua Sao Francisco Xavier, 524, 20550-013 Rio de Janeiro, RJ, Brazil*
[l] *University of Mississippi, Department of Physics and Astronomy, University, MS 38677, USA*
[m] *University of Nebraska-Lincoln, Lincoln, NE 68508, USA*
[n] *Florida State University, Tallahassee, FL 32306, USA*

Abstract

In preparation for the tenfold luminosity upgrade of the Large Hadron Collider (the HL-LHC) around 2020, three-dimensional (3D) silicon pixel sensors are being developed as a radiation-hard candidate to replace the planar ones currently being used in the CMS pixel detector. This study examines an early batch of FBK sensors (named ATLAS08) of three 3D pixel geometries: 1E, 2E, and 4E, which respectively contain one, two, and four readout electrodes for each pixel, passing completely through the bulk. We present electrical characteristics and beam test performance results for each detector before and after irradiation. The maximum fluence applied is 3.5x10^{15} n$_{eq}$/cm^2.

Keywords: 3D, CMS, pixel detector, HL-LHC, radiation-hard

1. Introduction

Radiation-hard tracking detectors are being developed for Large Hadron Collider (LHC) experiments to withstand the increased radiation level expected from the High-Luminosity LHC (HL-LHC) upgrade, which will take place around 2020. The detectors currently in use in the innermost barrel layer of the CMS pixel tracker will collect fluences up to the order of 10^{15} n$_{eq}$/cm^2 in their lifetime. After the HL-LHC upgrade, the new detectors in this layer are estimated to receive ten times this amount [1]. The current planar pixel sensors are not designed to withstand this amount of radiation [2]. Three-dimensional (3D) silicon pixel detectors are a promising radiation-hard alternative [3].

*Corresponding author
Email address: akrzywda@purdue.edu (A. Krzywda)

Preprint submitted to Elsevier *May 14, 2014*

3D sensors possess cylindrical electrodes that pass vertically through the bulk. This technology was first introduced in 1997 [4], and has the advantage that inter-electrode distance is independent from substrate thickness (Figure 1). This creates superior features: higher electric fields between the electrodes means lower depletion voltages, and shorter charge carrier drift distance speeds up charge collection and increases radiation hardness, therefore improving signal efficiency in irradiated sensors. The drawbacks of 3D technology compared to planar are: complex processing procedures, increased noise due to higher pixel capacitance, and lower efficiency in some low-field regions between electrodes of the same doping type.

The first full 3D sensors were fabricated at Stanford [5]. The fabrication process was developed further at SINTEF (Oslo, Norway) for larger-scale production [6], [7]. To simplify the fabrication process, double-sided processing was developed independently at both Fondazione Bruno Kessler (FBK) in Trento, Italy [8], and CNM-IBM in Barcelona, Spain [9].

The 3D sensors considered in this study are "Double-side Double-type Column" (3D-DDTC), from the batch ATLAS08, fabricated at FBK. Readout (n+) electrodes are etched from the front side, while ohmic (p+) electrodes are etched from the back. In the original 3D-DDTC process at FBK, electrodes did not pass through the silicon bulk, resulting in low-field regions between the tip of the columns and the surface. In addition, calibration of the deep-reactive ion etching (DRIE) process to obtain the desired depth was difficult and prone to create differences in electrode overlap [10].

The sensors considered in this study are part of the second generation of FBK 3D-DDTC sensors having passing-through electrodes [11]. The devices are electronically characterized before being placed in a beam at FNAL, both before and after proton irradiation. Similar studies of FBK 3D detectors have been done by the ATLAS collaboration [12], on sensors from different wafer batches. The ATLAS Insertable B-Layer, to be installed during the current LHC shutdown, will be partially instrumented with 3D sensors, thanks to these characteristics [13], [14].

2. 3D detectors

The sensors are fabricated on Float Zone p-type high-resistivity wafers, thickness 200 $\pm$ 20 μm. All columns pass completely through the silicon bulk. The electrodes are hollow, with metal contact made to the wafer surface by small planar diffusion. The surface isolation of electrodes is accomplished by p-spray implantations on both wafer sides as shown in Figure 1.

These 3D devices house a standard edge region about 1 mm wide, with planar guard rings surrounding the active area. Double-sided sensors do not have an active edge, as that requires a support wafer which would make the backside inaccessible. The dead area has been decreased to 200 μm or less in recent production batches at FBK by implementing "slim-edge" technology [15]. More detailed information on 3D-DDTC can be found in [11].

Each 3D sensor is read out using the PSI46v2 read-out chip (ROC) [16]. The sensors are diced and bump-bonded to the ROC with indium bumps at SELEX (Italy). The ROC has 4160 read-out pixels arrayed as 52 columns $\times$ 80 rows, with pitch 150 μm and 100 μm, respectively.

Three different 3D pixel configurations, 1E, 2E, and 4E, have been tested. The numbers in "1E," "2E," and "4E" refer to the number of readout electrodes in each pixel. Each n+ electrode is surrounded by six p+ electrodes in the 1E configuration and four p+ electrodes in the 2E and 4E configurations (Figure 1). The inter-electrode distance (the diagonal length between an n+ electrode and its nearest corner p+ electrode) for the 1E, 2E, and 4E configurations are 90 μm, 62.5 μm, and 45 μm, respectively. For 1E sensors, although the inter-electrode distance refers to the diagonal electrode separation, there are p+ columns 50 μm from the n+ in the short-pitch direction to reduce low-field regions between the n+ electrodes of neighboring pixels.

Assembly is performed in the P3MD lab at Purdue University and in the INFN laboratories in Turin, Italy. The assembly procedure is similar to that of the CMS forward pixel detector modules as described in [17]. Bump-bonded ROCs are glued and wire-bonded to a very high density interconnect (VHDI) circuit, which in turn is wire-bonded to a fan-out board. The fan-out board and VHDI are glued to a base plate (Figure 2).

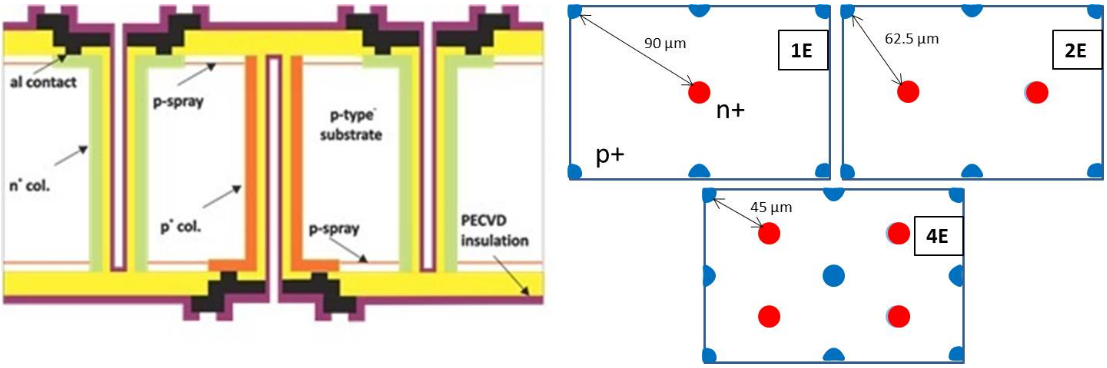

Figure 1: Left: 3D cross section. Electrodes are etched from either side and pass completely through the bulk. Right: Top-down view of FBK 1E, 2E, and 4E configurations.

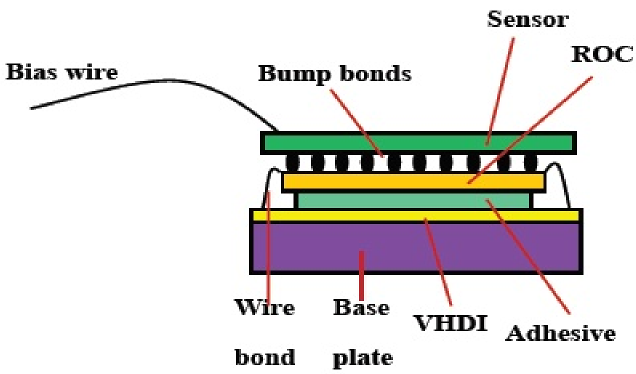

Figure 2: Artistic model of 3D assembly components. Each sensor is bump-bonded to a ROC, which is in turn connected to the DAQ system through a VHDI.

3. Sample preparation and experimental setup

The laboratory test stand consists of a PSI46 DAQ board connected to a PC. The DAQ board has an FPGA, a 12-bit ADC, and a 64 MB SDRAM buffer. The board and corresponding software were developed to qualify detectors using the PSI46v2 ROC [18]. An Agilent E3631A power supply provides voltage to the board. A Keithley 2410 source meter is used to bias the sensors and measure leakage current. For measurements that require cooling, the detector is placed inside a humidity-controlled cooling chamber.

3.1. Irradiation

Sensors are irradiated at the Los Alamos LANSCE facility. The average flux per macro-pulse for a 1 cm^2 sample is 2.33×10^{11} 800 MeV protons. The 1 MeV neutron equivalent NIEL damage factor for 800 MeV protons is 0.71 [19]. Obtained fluences are 7×10^{14} n_{eq}/cm^2 and 3.5×10^{15} n_{eq}/cm^2 (henceforth denoted 7E14 and 3.5E15 n_{eq}/cm^2). Due to laboratory procedure at Los Alamos, the sensors are left at room temperature for about one hour after irradiation before being transferred to a refrigerator at -20 °C. Other than this, no annealing is applied to the sensors after irradiation.

3.2. Beam Tests

The sensors are tested with 120 GeV protons at the Fermilab meson test beam facility. No magnetic field is applied. Devices under test (DUTs) are placed in pairs inside a telescope tracker (Figure 3). The trigger signal is provided by two PMTs coupled to scintillators downstream from the telescope.

The telescope consists of eight tracking planes – four 2x3 and four 2x4 planar modules for the CMS forward pixel detector. Pixels in each chip are arranged in 52 columns with pitch 150 μm (local x-axis) by 80 rows with pitch 100 μm (local y-axis), the same as the 3D chips to be tested. The 2x3 and 2x4 planes are oriented perpendicular to one another and rotated 25 degrees about their local x-axes to increase charge sharing and improve the tracking resolution in the local y-coordinate (Figure 4). More detailed information on the telescope can be found in [20].

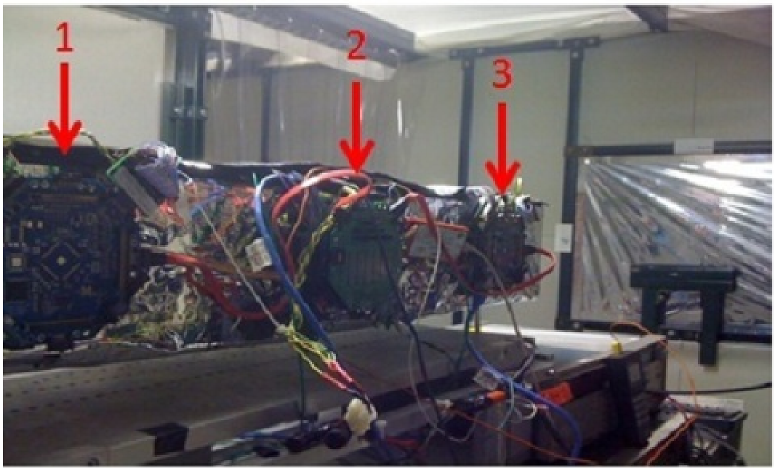

Figure 3: Photo of the telescope. There are three CAPTAN DAQ boards mounted on the telescope frame: one for the downstream detectors (1), DUTs (2), and upstream detectors (3).

The 3D sensors are enclosed in a thermally isolated box with water-cooled Peltier elements for sensor cooling. The internal humidity and temperature of the box are monitored with a sensor mounted near the DUT. The box itself is mounted on top of a remotely controlled rotary stage inside the telescope enclosure. Temperature and angle are set remotely through a PC connection.

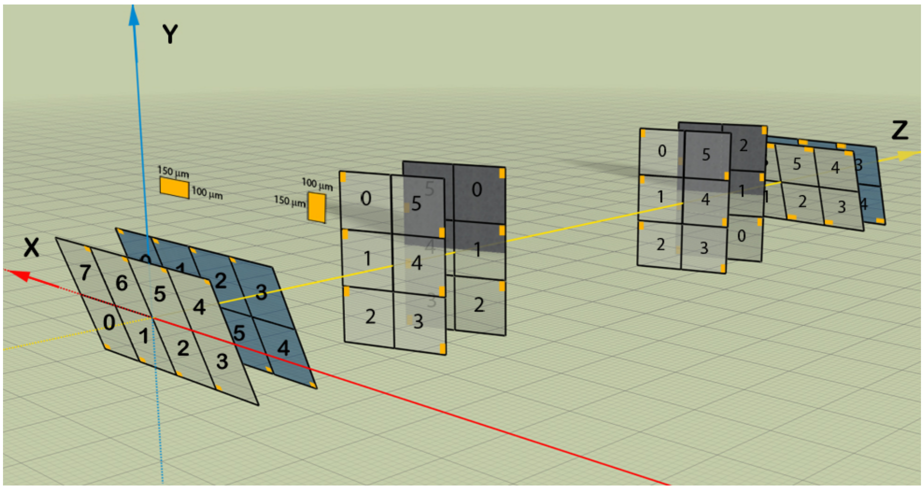

Figure 4: Geometrical layout of the telescope planes.

Data acquisition is controlled through CAPTAN, a DAQ system developed at FNAL [20]. CAPTAN employs a gigabit Ethernet connection which allows for remote control of the entire DAQ system from the test beam control room. The upstream telescope, downstream telescope, and DUTs are each attached to their own physical CAPTAN board. ROC voltages and settings are controlled through CAPTAN DAQ software.

Sensor charge collection, efficiency, and resolution are studied by independently varying bias, threshold, and angle. The sensors' optimal threshold and bias are determined immediately preceding the data taking process. Tracks are reconstructed for each event before determining efficiency and resolution. The telescope can achieve a track resolution as low as 6 μm [21].

4. Results and analysis

4.1. IV measurements

Leakage current (Figures 5 and 6) is measured with a Keithley source meter before and after irradiation to determine breakdown voltage. All devices experience breakdown between -20V and -40V bias. This is typical for FBK CMS 3D sensors [22]. It is difficult to determine the exact point of breakdown for many of the sensors, which is likely due both to soft breakdowns around local bulk defects, and systematic error (such as short time between measurements). A significant increase in breakdown voltage after irradiation is not clearly seen. Before and after irradiation, respectively, the instrument compliance is 99 μA and 505 μA; the results are normalized to -20 °C.

There are notable discrepancies between lab and simulation results. The high leakage current and early breakdown in the real sensors are due to process-related defects. Fabrication-induced defects could not be incorporated into the simulations and are a major cause of the discrepancies between the real and simulated currents. These defects are now understood and have been improved in more recent batches [23].

4.2. Noise

Noise is determined by injection efficiency measurements, which are described in detail in [6]. The readout efficiency for each pixel is found using internal charge injection via the chip, and the data is fitted with an error function (S-curve). The width of the S-curve corresponds to the pixel noise. Noise measurements are taken at room temperature before irradiation, and -20 °C after irradiation. The results are based on single measurements. They are shown in Figure 7.

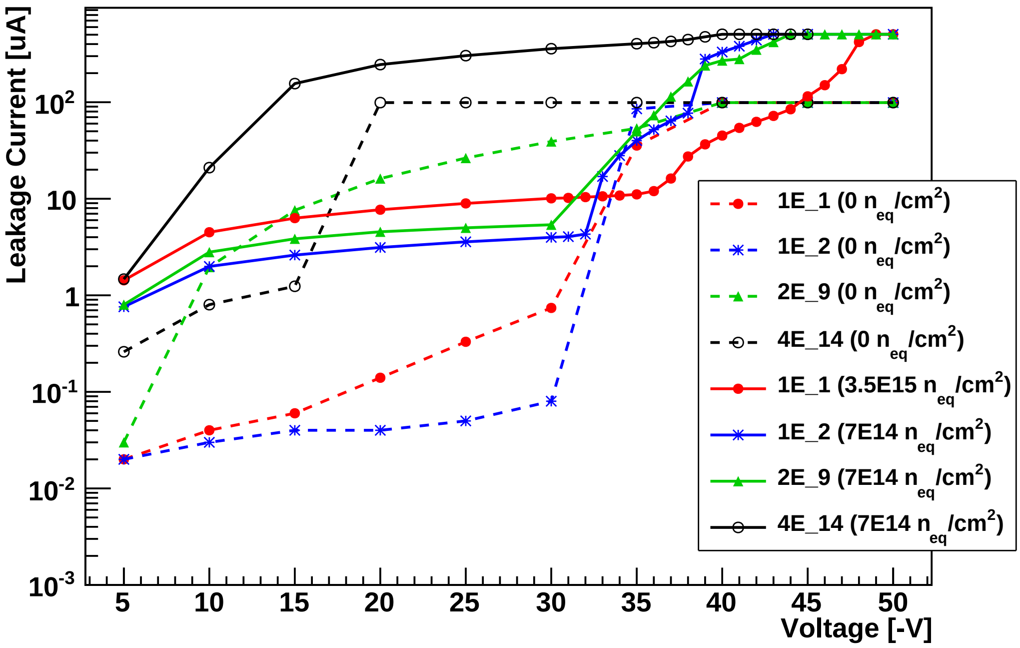

Figure 5: Laboratory IV measurements before and after irradiation.

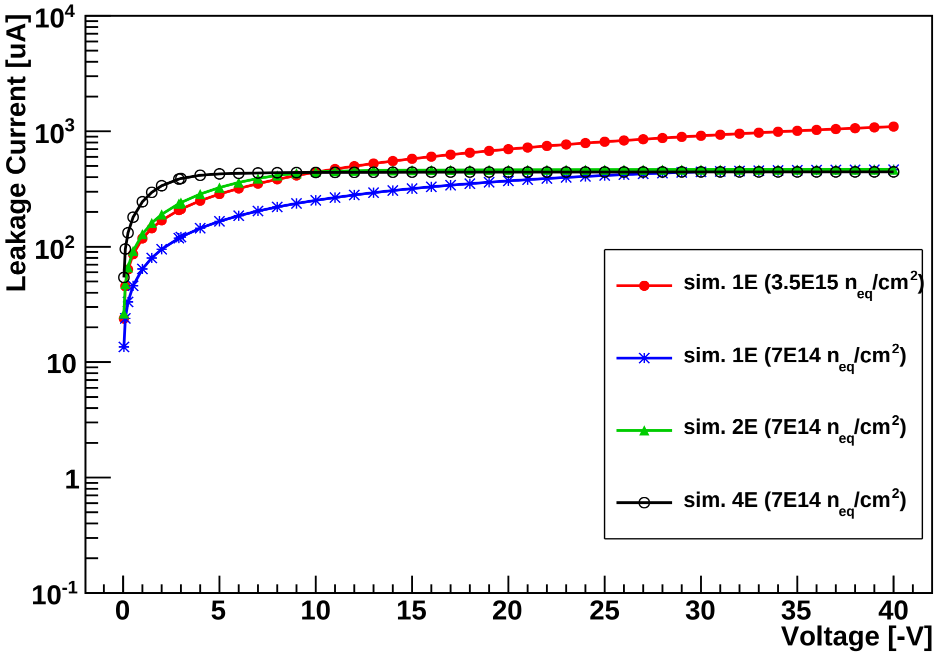

Figure 6: Simulated IV of irradiated sensors.

The sensor noise is related to pixel capacitance (electrode spacing) and irradiation level, among other factors. After irradiation, the noise increases by 20-30% in the 1Es and around 10% in the 2E. The 4E_14 does not experience the same noise behavior as the other sensors, though conclusions about this behavior are difficult to draw due to the low statistics.

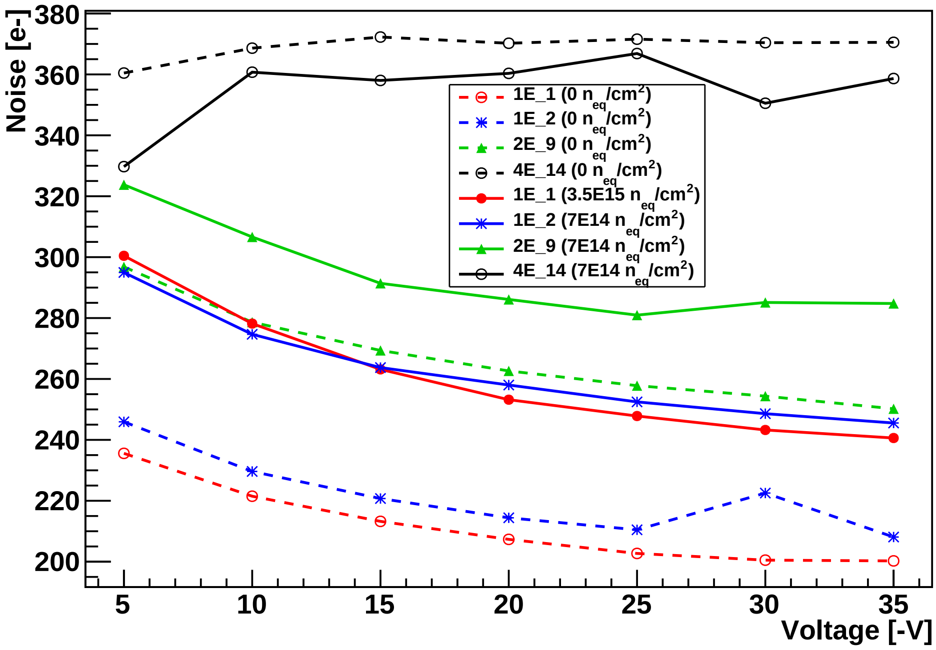

Figure 7: Noise as a function of bias before and after irradiation.

4.3. Test beam data analysis

Event data from the test beam are analyzed using software developed specifically for the Fermilab test beam. Charge is measured directly by the readout chip. Efficiency and resolution are calculated after iterative alignment of the telescope and DUTs. Due to limited data, pre-irradiation results are shown for the sensor 4E_12, while post-irradiation results are shown for the sensor 4E_14. Similarly, bias scan results are presented for the sensor 2E_11 before irradiation, and for the sensor 2E_9 after irradiation. All sensors are from the same batch.

4.3.1. Charge collection – simulations and beam tests

Charge is read out in analog by the ROC directly, which is then converted into digital units after electronic calibration. The distribution of electron charge collected by the sensor over a set of events is a Landau curve convoluted with a Gaussian due to noise spreading. The charge is taken as the most probable value (MPV) of the distribution because the MPV is minimally affected by noise, and is ideally a constant for ionizing particles of charge ±1. For a perfectly charge-efficient sensor, the charge collected is 80 electrons per μm of substrate thickness.

Simulation model and domain

TCAD simulations are performed to model the charge collection of irradiated sensors. The simulation assumes a single incident particle passing normally through a particular point on a pixel. Specifically, the simulation point is located halfway between an n+ electrode and its nearest corner bias electrode. For 1E-type sensors, a second simulation is performed close to the readout. These coordinates are hereby referred to as "center" and "electrode," respectively. Simulation domains and coordinates are illustrated in Figure 8.

The simulations are carried out by solving continuity and Poisson equations simultaneously, including carrier drift, diffusion, generation, and recombination using Shockly-Read-Hall statistics and avalanche generation. A small characteristic section of the pixel cell is simulated, and then scaled to the full size of the device.

A substrate thickness of 200 μm and electrode diameter of 12 μm is used. The substrate is p-type with a doping concentration of 7×10^{11} cm^{-3}, corresponding to a resistivity of ~ 20 k$\Omega \cdot$ cm. The doping concentration of all electrodes is assumed to be 5×10^{19} cm^{-3}. All parameters are representative of FBK technology.

The model used to simulate the devices is the University of Perugia proton radiation damage model for p-type FZ silicon, with modified parameters [24], [25]. The model consists of three trap levels with two acceptor levels and one donor. The two acceptor levels, positioned slightly above the midpoint of the band gap, increase leakage current, change the effective doping concentration, and trap excess electrons from the conduction band. The donor level is farther away from the midpoint and serves to trap excess holes from the valence band.

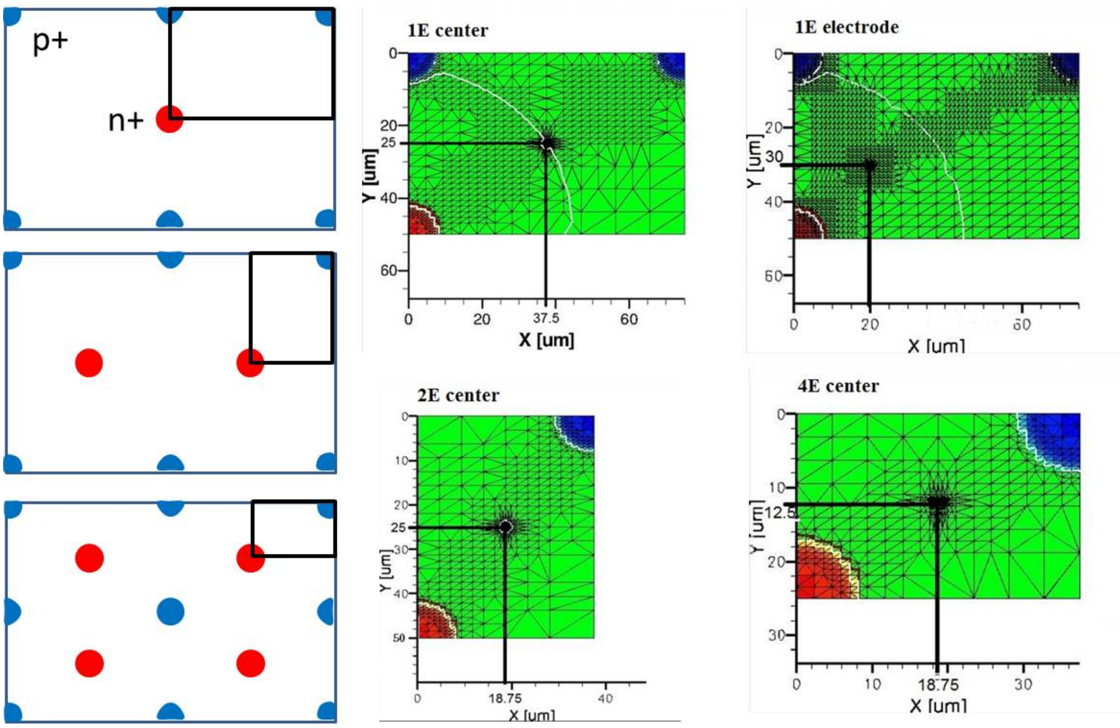

Figure 8: Simulation domains. In the figures on the right, green denotes bulk material, red a readout electrode, and blue a bias electrode.

Pre-irradiation charge collection

Figure 9 shows the collected charge (MPV) of sensors before irradiation. Results are extracted from testbeam data. Full depletion is achieved at relatively low bias in unirradiated devices, as evidenced by the drop-off below 10 V in the 1E sensors. In the 4E, full depletion occurs at even lower bias. The charge asymptotically approaches 16 ke^{-} for the 1E_1 and 14 ke^{-} for the 1E_2, approximately. The charge collected by the 4E_12 is about 12.5 ke^{-} and is nearly constant with applied bias.

Post-irradiation charge collection

Experimental charge values are compared to simulation data in Figures 10 and 11. The testbeam data reproduces the simulation results very well in the electrode region. A threshold of 6 ke$^-$ is applied in the analysis – any charge less than this was discarded. Such a large threshold is chosen due to the high level of noise in the detectors. The effect of carrier trapping is readily apparent in the 1E irradiated to 3.5E15 n_{eq}/cm^2. At low applied voltages, charge collection is almost nonexistent at the "center" coordinate. Very little charge is collected even at larger voltages. By contrast, the "electrode" region does not see this effect, implying particles are only detectable in the immediate area around the readout. These effects are only seen in irradiated sensors, where significant charge trapping occurs. The area of the charge collection-efficient region can, in theory, be improved by increasing the number of readout electrodes, which serves to increase the electric fields within the bulk and decrease the charge carrier drift distance. Charge collection studies on highly irradiated 2E and 4E sensors are foreseen.

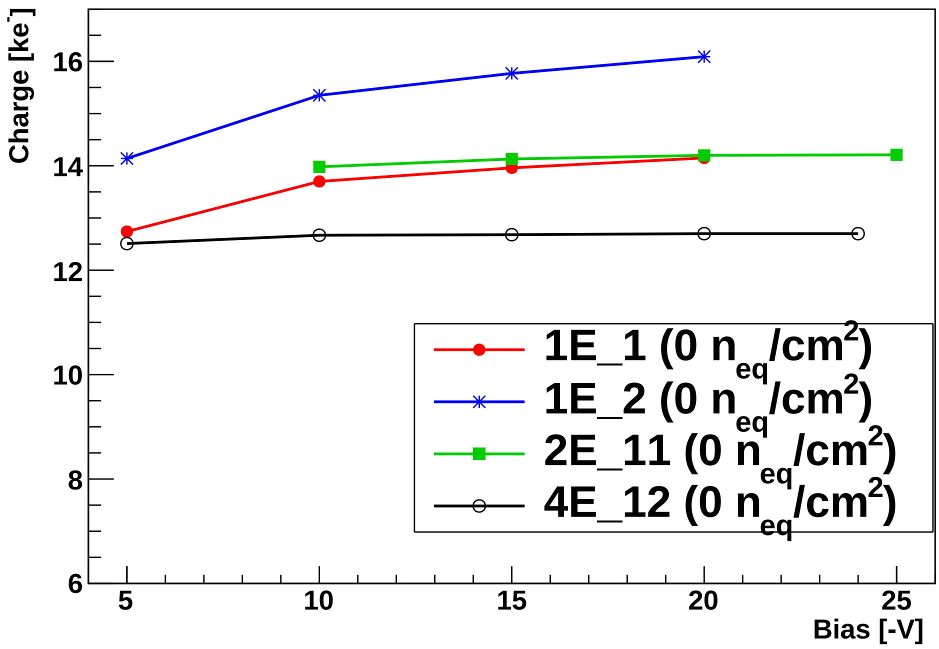

Figure 9: Charge (MPV) versus reverse bias voltage for unirradiated sensors.

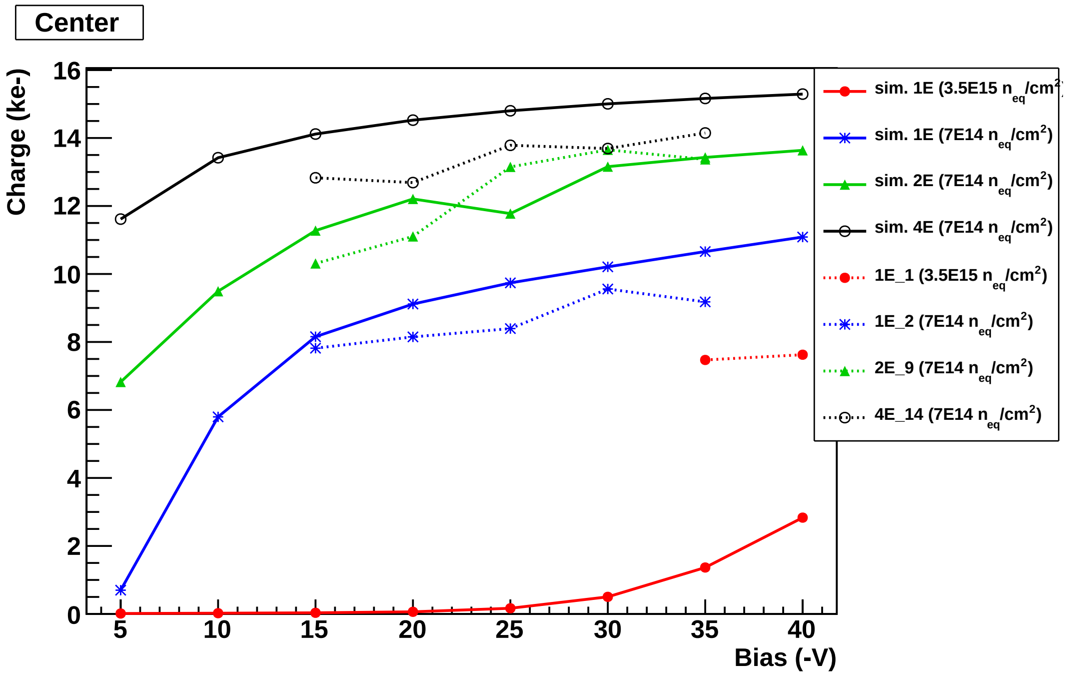

Figure 10: Charge (MPV) collected midway between the n+ and corner p+ electrodes, with simulations.

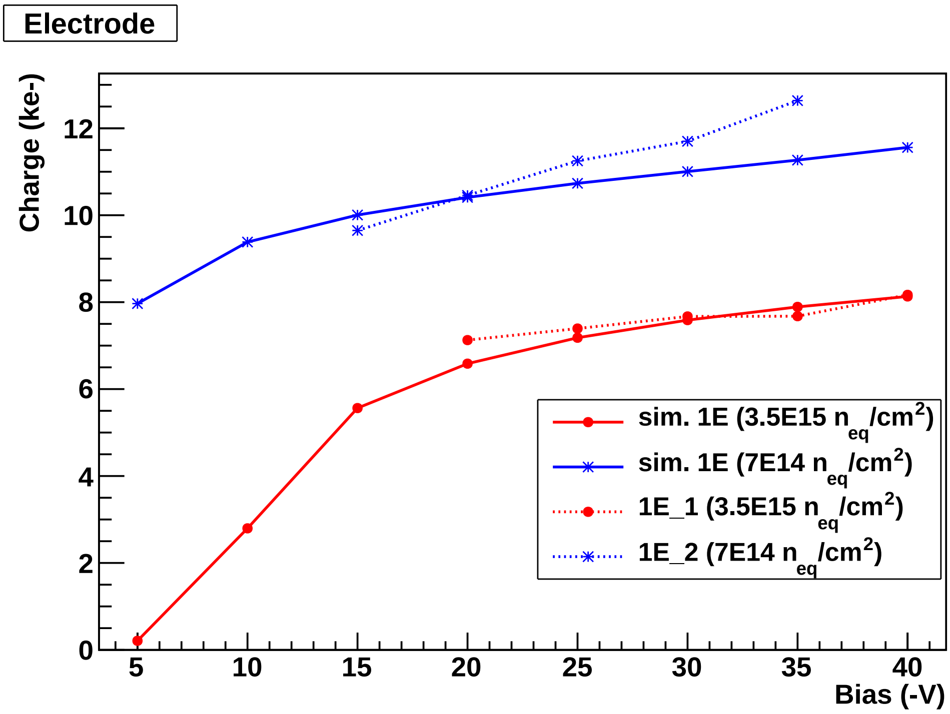

Figure 11: Charge (MPV) collected near the n+ readout electrodes, with simulations.

4.3.2. Tracking efficiency

Tracks are reconstructed by the following method: hits lying within a window of one pixel area around the direction defined by the line going through a pair of hits on the first and last planes of the telescope are used to perform a linear fit in space. Events must have hits in all eight telescope planes. DUT events with more than one track are rejected. Efficiency is studied at normal beam incidence to the sensor plane.

Tracking efficiency is determined on an event-by-event basis on the DUT. An event's efficiency is equal to one if a hit is registered within one pixel area of a reconstructed track and zero otherwise. The total sensor efficiency is determined by normalizing the efficiency of all events in a given run. The efficiency is strongly affected by the telescope track error, charge trapping, bias, and threshold. Tracking efficiency is also limited by the dead area inside the electrode columns. The area filled by an electrode cannot be used to track particles.

Figure 12 shows efficiency versus bias voltage. Operational bias voltages are determined from this data before scanning for optimum thresholds. The 1E_1 sees nearly 60% efficiency loss after irradiation to 3.5E15 n_{eq}/cm^2. The 2E_9 gives the best performance after irradiation, achieving over 90% efficiency. Tracking efficiency falls after approximately -30V due to breakdown in some sensors.

Figure 13 is a plot of tracking efficiency versus readout threshold. Threshold is displayed in arbitrary DAC units. Approximate electron values are calculated at peak efficiency, given in Table 1. Efficiency rises as the threshold decreases, until eventually the noise becomes too great for the chip to distinguish between real hits and noise and the sensor efficiency drops. Radiation-induced traps also degrade the signal, causing a drop in tracking efficiency due to a decreased signal-to-noise ratio. Efficiency loss after irradiation is greatest in the highly irradiated 1E_1 and smallest in the 2E_9. The relative losses due to irradiation are also given in Table 1.

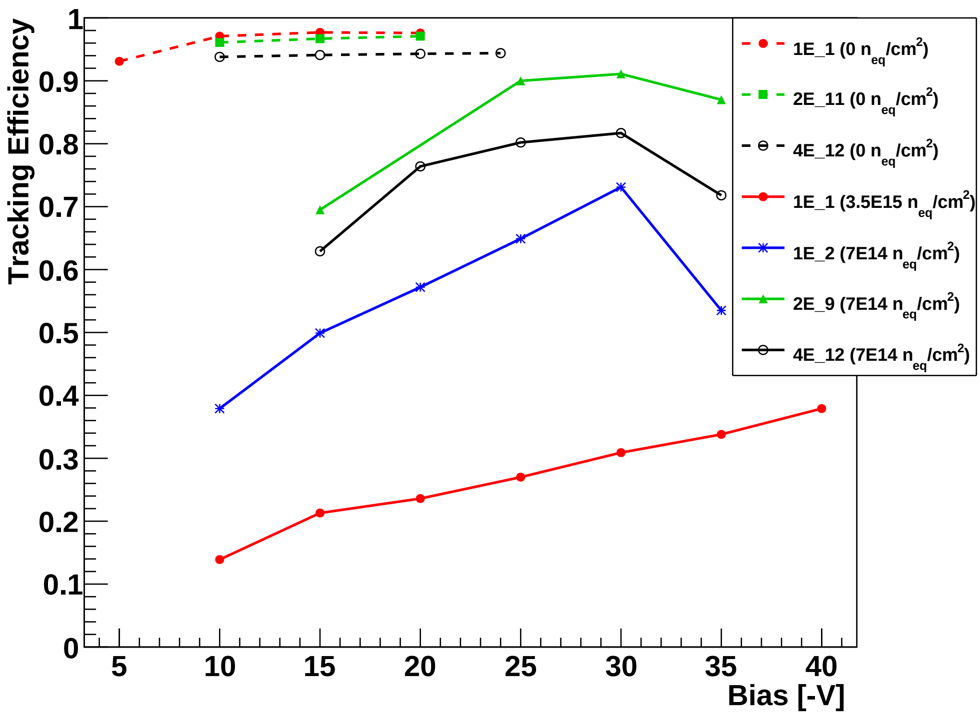

Figure 12: Tracking efficiency versus bias.

Sensor (fluence [n_{eq}/cm^2])	Peak efficiency	Relative efficiency loss	Bias [-V]	Threshold [e^-]
1E_1 (0)	97.8%	n/a	15	4000
1E_2 (0)	97.6%	n/a	15	5600
2E_9 (0)	95.4%	n/a	5	6300
2E_11 (0)	97.8%	n/a	15	unknown
4E_12 (0)	94.5%	n/a	15	6000
1E_1 (3.5E15)	37.9%	61.2%	40	4900
1E_2 (7E14)	73.1%	25.1%	30	4300
2E_9 (7E14)	91.1%	4.5%	30	5000
4E_14 (7E14)	81.7%	n/a	30	6200

Table 1: Maximum tracking efficiency before and after irradiation. Threshold conversion is not available for the 2E_11.

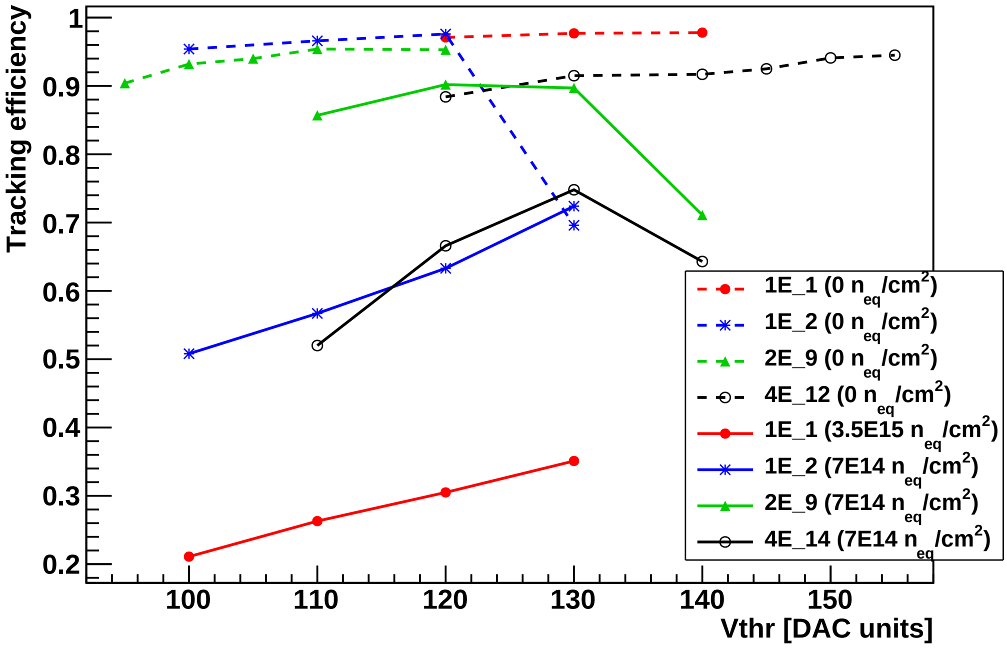

Figure 13: Tracking efficiency versus threshold.

4.3.3. Position resolution

Track residuals - the distance between the predicted and measured positions of a cluster - are calculated along the short-pitch direction. The residuals are fitted with a Gaussian; the overall sensor resolution is determined from the sigma of the fit (Figure 14). The error from the telescope is subtracted during the analysis. For single-hit clusters the residual is the width of the pixel. Better resolution is obtained when charge is shared between pixels. In this case, residuals are taken only for 2-pixel clusters. In the CMS barrel, charge sharing is achieved through a combination of detector tilt and a 4 T magnetic field. The test beam DUTs are tilted to various angles to emulate these effects.

Residuals for irradiated sensors can be improved through studies of charge versus x/y cluster position (charge asymmetry) averaged over each pixel. This is done on the first DUT alignment. Residuals are improved by reiterating the alignment procedure and using the measured charge to determine cluster positions directly from the asymmetry plot. This will be implemented in future 3D studies.

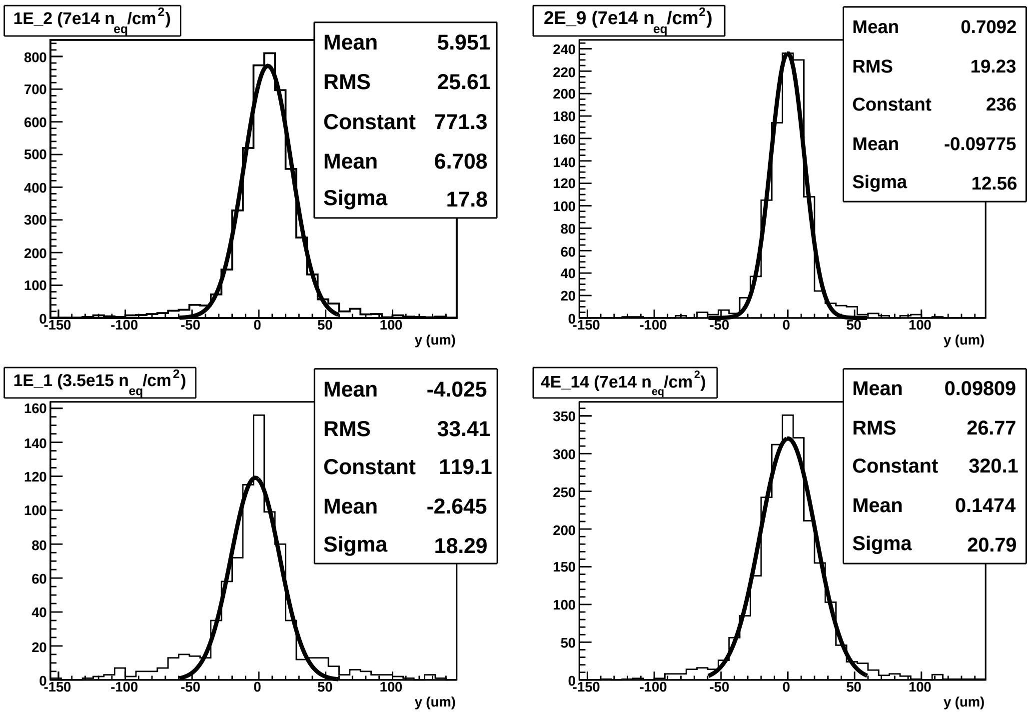

Figure 14: Irradiated sensor residuals for size two clusters, with Gaussian fit. Top left: 1E_2 (17.8 μm); top right: 2E_9 (12.56 μm); bottom left: 1E_1 (18.29 μm); bottom right: 4E_14 (20.79 μm). Note that the 1E_1 data provided low statistics.

5. Summary and Conclusions

3D tracking detectors are a promising radiation-hard candidate to replace planar detectors in the HL-LHC where the innermost barrel sensors must withstand a fluence of approximately 10^{16} n_{eq}/cm^2. Electrical and beam tests were performed for FBK ATLAS08 3D detectors before and after irradiation. The detectors were bump-bonded at SELEX, Italy, and assembled and wired at the P3MD lab at Purdue University. Three of the detectors were irradiated to 7E14 n_{eq}/cm^2, and one to 3.5E15 n_{eq}/cm^2. Radiation damage effects are demonstrated with regards to charge collection, efficiency, and resolution of the particle tracks in beam tests, as well as leakage current and pixel noise. After irradiation, the 2E showed the least degradation of charge and efficiency. Lab and test beam studies are ongoing for more recent batches from FBK, with improved fabrication processes.

Acknowledgments

This work was funded by the U.S. Department of Energy under Grant DE-FG02-91ER40681, the National Science foundation under Cooperative Agreement PHY 0612805 UCLA Subaward 1000 G HD 870, the Provincia Autonoma di Trento through the Project MEMS2, and also by the Italian National Institute for Nuclear Physics (INFN) through the CSN5 Project TREDI.

The PSI46v2 ROCs were developed by R. Horisberger's research group (W. Erdmann, R. Horisberger, H.C. Kästli, and B. Meier) at the Paul Scherrer Institute in Switzerland.

References

[1] Silicon Strip Detectors for the ATLAS HL-LHC Upgrade, Physics Procedia vol. 37 (2012) pp. 915-922, ISSN 1875-3892. http://dx.doi.org/10.1016/j.phpro.2012.02.429

[2] Caminada, Lea, *Recent Developments of HEP Pixel Detector Readout Chips*, Physics Procedia vol. 37 (2012) pp. 1644-1653, ISSN 1875-3892. http://dx.doi.org/10.1016/j.phpro.2012.02.488

[3] Paula Collins, *Semiconductor detectors for high-luminosity environments*, Nucl. Inst. and Meth. A 581 (2007) p. 38. http://dx.doi.org/10.1016/j.nima.2007.07.023

[4] S. I. Parker et al., *3D - A proposed new architecture for solid-state radiation detectors*, Nucl. Instr. and Meth. A 395 (1997) p. 328. http://dx.doi.org/10.1016/S0168-9002(97)00694-3

[5] C. Kenney et al., *Silicon detectors with 3-D electrode arrays: fabrication and initial test results*, IEEE Trans. Nucl. Sci., vol. 46, no. 4, pp. 1224-1236, 1999. http://dx.doi.org/10.1109/23.785737

[6] O. Koybasi et al., *Electrical Characterization and Preliminary Beam Test Results of 3D Silicon CMS Pixel Detectors*, IEEE Trans. Nucl. Sci., vol. 55, no. 5, pp. 2775-2784, 2008. http://dx.doi.org/10.1109/TNS.2011.2117439

[7] T.E. Hansen et al., *First fabrication of full 3D-detectors at SINTEF*, 2009 JINST 4 P03010. http://dx.doi.org/10.1088/1748-0221/4/03/P03010

[8] A. Zoboli et al., *Double-sided, Double-Type Column 3-D Detectors: Design, Fabrication and Technology Evaluation*, IEEE Trans. Nucl. Sci., vol. 55, no. 5, pp. 2775-2784, 2008. http://dx.doi.org/10.1109/TNS.2008.2002885

[9] G. Pellegrini et al., *First double-sided 3-D detectors fabricated at CNM-IMB*, Nucl. Instr. and Meth. A 592 (2008) p. 38. http://dx.doi.org/10.1016/j.nima.2008.03.119

[10] A. La Rosa et al., *Characterization of proton irradiated 3D-DDTC pixel sensor prototypes fabricated at FBK*, Nucl. Instr. and Meth. A 681 (2012) pp. 25-33. http://dx.doi.org/10.1016/j.nima.2012.03.048

[11] G. Giacomini et al., *Development of double-sided full-passing-column 3D sensors at FBK*, IEEE Trans. Nucl. Sci., NS-60(3), pp. 2405-2410, 2013. http://dx.doi.org/10.1109/NSSMIC.2010.5873785

[12] A. Micelli et al., *3D-FBK pixel sensors: Recent beam tests results with irradiated devices*, Nucl. Inst. and Meth. A 650 (2011) p. 150. http://dx.doi.org/10.1016/j.nima.2010.12.209

[13] The ATLAS IBL Collaboration, *Prototype ATLAS IBL Modules using the FE-I4A Front-End Readout Chip*, JINST 7 (2012) P11010.

[14] C. Da Via et al., *3D Silicon Sensors: Design, Large Area Production and Quality Assurance for the ATLAS IBL Pixel Detector Upgrade*, Nucl. Instr. and Meth. A 694 (2012) p. 321.

[15] M. Povoli et al., *Slim edges in double-sided silicon 3D detectors*, 2012 JINST 7 C01015. http://dx.doi.org/10.1088/1748-0221/7/01/C01015

[16] W. Erdmann, *The 0.25 μm front-end for the CMS pixel detector*, Nucl. Instr. and Meth. A 549 (2005) 153. http://dx.doi.org/10.1016/j.nima.2005.04.044

[17] O. Koybasi et al., *Assembly and qualification procedures of CMS forward pixel detector modules*, Nucl. Instr. and Meth. A 638 (2011) 55. http://dx.doi.org/10.1016/j.nima.2011.02.106

[18] A. Starodumov et al., *Qualification procedures of the CMS pixel barrel modules*, Nucl. Instr. and Meth. A 565 (2006) 67. http://dx.doi.org/10.1016/j.nima.2006.04.087

[19] A. Vasilescu and G. Lindstroem, *Displacement damage in silicon*, Online compilation, http://polzope.in2p3.fr:8081/ATF2/collected-information/displacement-damage-in-silicon-from-unno-san-kek/.

[20] R. Rivera et al., *A Telescope Using CMS PSI46 Pixels and the CAPTAN for Acquisition and Control over Gigabit Ethernet*, 2009 IEEE NSS, Conference record paper.

[21] S. Kwan et al., *The CMS Pixel Tracking Telescope at the Fermilab Test Beam Facility*, submitted for publication.

[22] E. Alagoz et al., *Simulation and laboratory test results of 3D CMS pixel detectors for HL-LHC*, 2012 JINST 7 P08023. http://dx.doi.org/10.1088/1748-0221/7/08/P08023

[23] M. Obertino et al., *3D-FBK pixel sensors with CMS readout: First test results*, Nucl. Instr. and Meth. A Proof (2012). http://dx.doi.org/10.1016/j.nima.2012.11.076

[24] M. Petasecca et al., *Numerical Simulation of Radiation Damage Effects in p-Type and n-Type FZ Silicon Detectors*, IEEE Trans. Nucl. Sci., vol.53, no.5, pp.2971-2976, Oct. 2006. http://dx.doi.org/10.1109/TNS.2006.881910

[25] D. Pennicard et al., *Simulations of radiation-damaged 3D detectors for the Super-LHC*, Nucl. Instr. and Meth. A 592 (2008) 16. http://dx.doi.org/10.1016/j.nima.2008.03.100

[26] P. Trub, *CMS pixel module qualification and Monte-Carlo study of* $H \to \tau^- \tau^- \to l^+ l^- E_T$, Ph.D. dissertation, ETH Zurich, Zurich, Switzerland, 2008.